An Enhancement of the NASA Team Sea Ice Algorithm

Thorsten Markus and Donald J. Cavalieri

Abstract—An enhancement of the NASA Team sea ice concentration algorithm overcomes the problem of a low ice concentration bias associated with surface snow effects that are particularly apparent in Southern Ocean sea ice retrievals. The algorithm has the same functional form as the NASA Team algorithm, but uses a wider range of frequencies (19–85 GHz). It accommodates ice temperature variability through the use of radiance ratios as in the original NASA Team algorithm, and has the added advantage of providing weather-corrected sea ice concentrations through the utilization of a forward atmospheric radiative transfer model. Retrievals of sea ice concentration with this new algorithm for both the Arctic and Antarctic do not reveal the deficiencies present in either the NASA Team or Bootstrap algorithms. Furthermore, quantitative comparisons with infrared AVHRR data show that the enhanced algorithm provides more accurate ice concentrations with much less bias than the other two algorithms.

Index Terms—Algorithms, passive microwave, sea ice.

I. INTRODUCTION

ACCURATE remote sensing of sea ice depends on knowing the emissivity of the ice, the physical temperature of the radiating portion of the ice, and the state of the atmosphere at the instant the ice is being observed. The difficulty is that these quantities are highly variable in space and time, particularly in the environment of the Arctic marginal seas and in the Southern Ocean. Sea ice emissivity depends on the physical, chemical, and electrical properties of the ice, properties that are determined by the environmental conditions in existence during the growth phase of the ice as well as by the prevailing conditions when the ice is observed. Differences in salinity, ice thickness, snow cover, and surface wetness are only some of the factors that contribute to variations in microwave emission. The physical temperature of the radiating portion of the ice depends on the air temperature and the snow cover that insulates the ice from the atmosphere. In winter, air temperatures over the Antarctic pack ice, for example, range from 240–270K (see Zwally *et al.*, [22, Figs. 2–7]), while snow conditions exhibit a variability from snow-free ice to ridged ice with a meter or more of snow.

Two widely used sea ice algorithms to derive sea ice concentrations from the DMSP SSM/I are the NASA Team (NT) algorithm [2], [7] and the Bootstrap (BS) algorithm [3]. Difficulties with both these algorithms have been described by Comiso *et al.* [4]. The comparative study revealed significantly

TABLE I
ANGLES IN RADIANS BETWEEN THE GR-AXIS AND THE A–B LINE (FY–MY LINE FOR THE ARCTIC) FOR THE $PR(19) - GR(37V\,19V)$ DOMAIN AND THE $PR(85) - GR(37V\,19V)$ DOMAIN

Hemisphere	ϕ_{19}	ϕ_{85}
Antarctic	−0.59	−0.40
Arctic	−0.18	−0.06

different sea ice concentrations of up to 30% in some parts of the Antarctic, with smaller although significant differences in parts of the Arctic. The study also identified potential reasons for the discrepancies, including the influence of sea ice temperature variability on the BS retrievals and the influence of ice surface reflectivity variability on the emissivity at horizontal polarization in the NT retrievals. The latter problem effectively results in the existence of an additional radiometrically different ice type. The use of the low (19–37 GHz) SSM/I frequencies by these and other algorithms [18] limits the algorithms to resolving at most two ice types, because of the high correlation of information content at these frequencies.

The challenge then was to find a combination of SSM/I channels that minimized the effects of ice type and ice temperature variability, while preserving a relatively large dynamic range to measure small changes in open water amount within the ice pack. We have taken the approach of revising the NT algorithm (the revised algorithm will be referred to as NT2), through the incorporation of the 85-GHz channels, while retaining both the relative insensitivity to ice temperature variations provided by radiance ratios and the relatively large dynamic range in sea ice concentration through the use of the 19-GHz channels. Mätzler *et al.* [15] have shown that the sensitivity to inhomogeneities of the surface layer on the horizontal polarization at 85 GHz is much reduced and therefore, they have suggested the use of the 85-GHz channels for ice concentration retrievals if one can handle its higher sensitivity to atmospheric effects compared to the 19-GHz and 37-GHz channels. Others have investigated the use of the 85-GHz channels to derive ice concentrations at a higher spatial resolution. Svendsen *et al.* [20] and Lubin *et al.* [12] used the 85-GHz data with a simplified radiative transfer model. They obtained good results when cloud contamination was small [12]. Others used the 85-GHz data in successive combination with the low frequency channels to retrieve high resolution ice concentration [17], coastal polynya areas [13] or sea ice edges [9], while correcting for atmospheric contributions in the 85-GHz data. In the algorithm presented here, this higher sensitivity to atmospheric effects is handled through forward calculations with a full atmospheric radiative transfer model [11].

TABLE II
MODEL ATMOSPHERES

| #	Season	Cloud type	LWC [g m^{-2}]	Base height [km]	Top height [km]
0	summer	clear	0.0	n/a	n/a
1	winter	clear	0.0	n/a	n/a
2	summer	cirrus	50.0	5.0	5.5
3	winter	cirrus	50.0	5.0	5.5
4	summer	stratus	15.0	0.4	0.7
5	winter	stratus	15.0	0.4	0.7
6	summer	stratus cumulus	75.0	0.5	1.0
7	winter	stratus cumulus	75.0	0.5	1.0
8	summer	stratus cumulus	125.0	0.5	1.0
9	winter	stratus cumulus	125.0	0.5	1.0
10	summer	cumulus congestus	250.0	1.0	3.0
11	winter	cumulus congestus	250.0	1.0	3.0
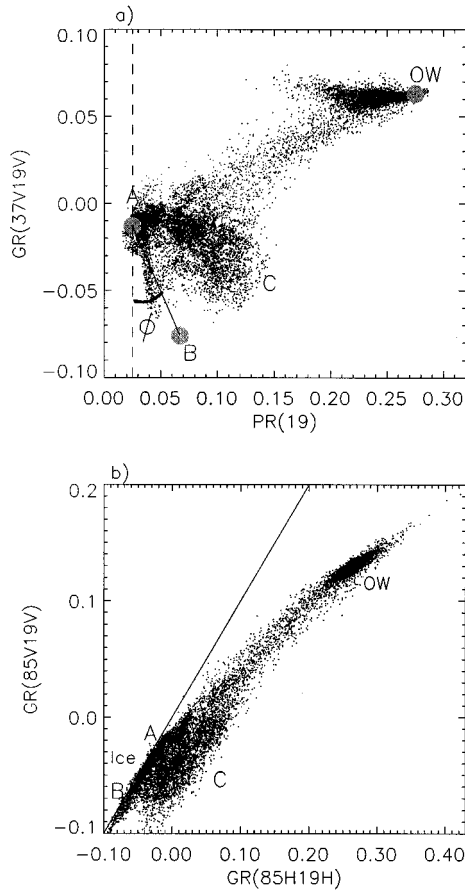
Fig. 1. (a) $GR(37V19V)$ versus $PR(19)$ for the Weddell Sea on September 15, 1992. The gray circles represent the tiepoints for the ice types A and B as well as for open water, as used by the NT algorithm. Label C indicates pixels with significant surface effects. ϕ is the angle between the y-axis and the A–B line. (b) $GR(85V19V)$ versus $GR(85H19H)$. The ice types A and B are close to the diagonal. The amount of layering corresponds to the horizontal deviation from this line toward label C.

Fig. 2. (a) ΔGR versus $PR_R(19)$ and (b) ΔGR versus $PR_R(85)$ for the same data set as in Fig. 1. The gray circles represent the modeled ratios for the three pure surface types with different atmospheric conditions.

II. DESCRIPTION OF THE ALGORITHM

The two ratios of brightness temperatures used in the standard NT algorithm as well as in the NT2 approach are the polarization

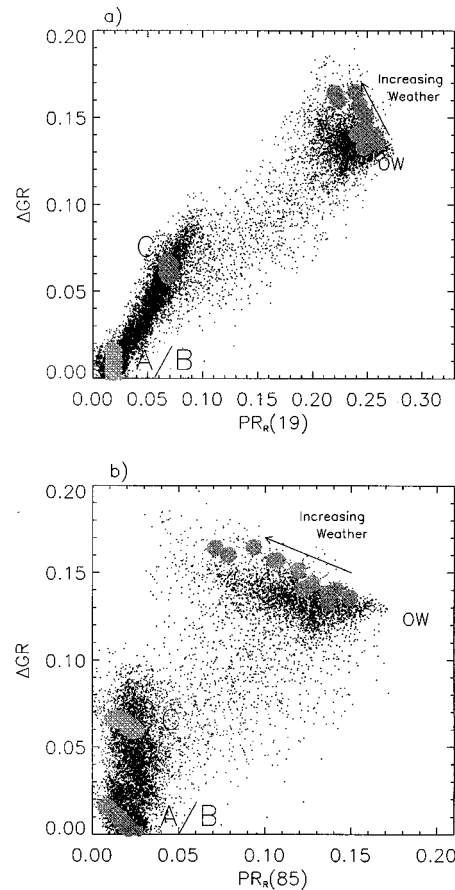$$PR(\nu) = \frac{TB(\nu V) - TB(\nu H)}{TB(\nu V) + TB(\nu H)} \tag{1}$$

and the spectral gradient ratio

$$GR(\nu_1 p \nu_2 p) = \frac{TB(\nu_1 p) - TB(\nu_2 p)}{TB(\nu_1 p) + TB(\nu_2 p)} \tag{2}$$

where TB is the brightness temperature at frequency ν for the polarized component p (vertical V or horizontal H).

Fig. 1(a) shows a typical scatterplot of $PR(19)$ versus $GR(37V19V)$ for September conditions in the Weddell Sea. The NT algorithm identifies two ice types associated with first-year and multiyear ice in the Arctic and ice types A and B in the Antarctic [as shown in Fig. 1(a)]. The A–B line
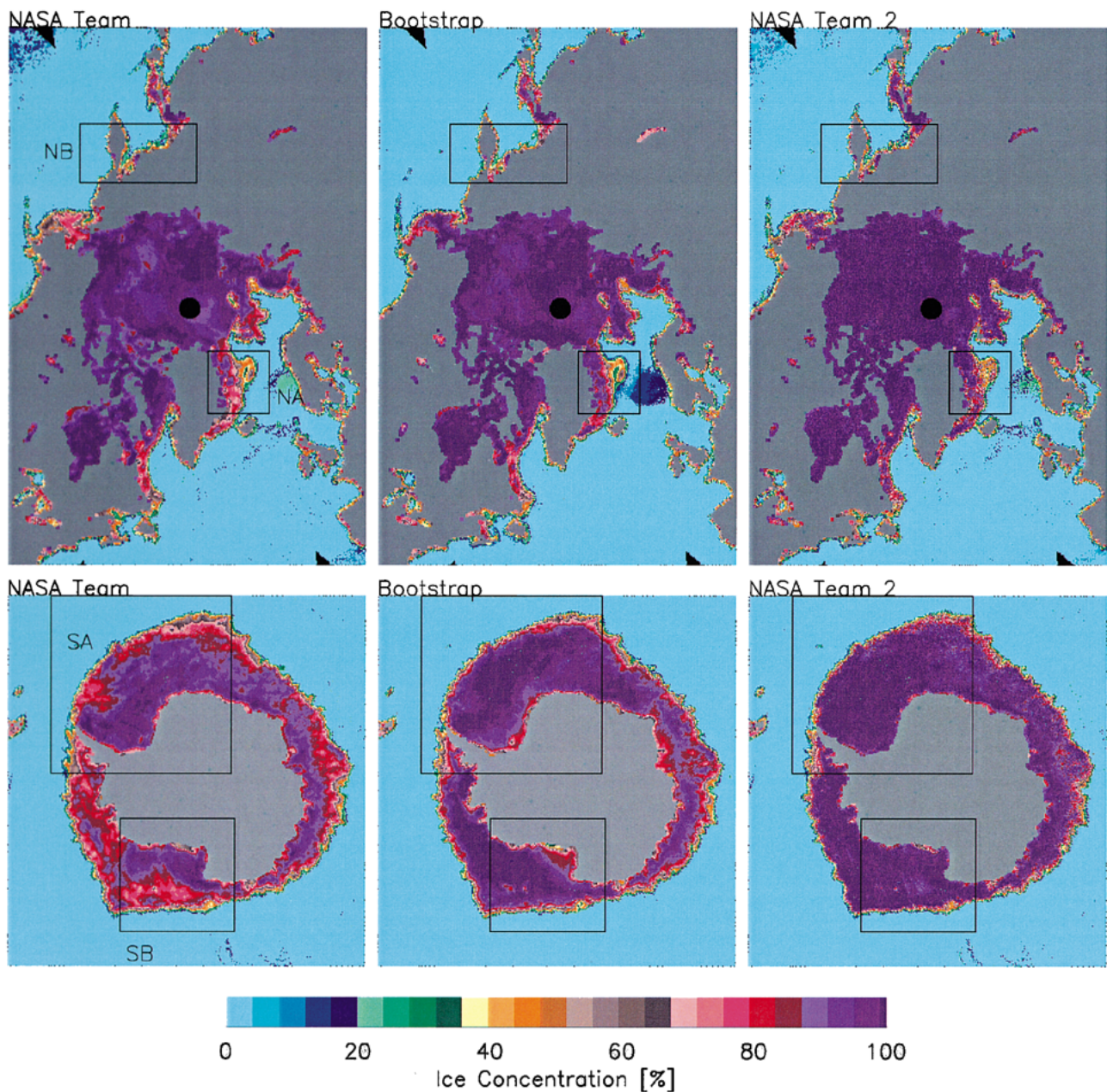
Fig. 3.   Top row: Ice concentration retrievals for the Arctic on January 27, 1997 using the NASA Team, the Bootstrap, and the enhanced NASA Team 2 algorithms. The boxes labeled NA and NB indicate subsets that are used for validation in Section IV. Bottom row: Ice concentration retrievals for the Antarctic on August 23, 1993 using the NASA Team, the Bootstrap, and the enhanced NASA Team 2 algorithms. The boxes labeled SA and SB indicate subsets that are used for validation in Sections III and IV.

represents 100% ice concentration. The distance from the open water point (OW) to line A–B is a measure of the ice concentration. In this algorithm, the primary source of error is attributed to conditions in the surface layer such as surface glaze and layering [4], which can significantly affect the horizontally polarized 19-GHz brightness temperature [15], leading to increased $PR(19)$ values and thus underestimate ice concentration. In the following, we will call these surface effects. In Fig. 1(a), pixels with significant surface effects create a cloud of points underestimating ice concentrations (labeled C). For this reason, the BS algorithm uses primarily the 19- and 37-GHz vertically polarized channels and uses only selectively the 37-GHz horizontally polarized channel.

The use of the SSM/I horizontally polarized channels makes it imperative to resolve a third ice type to overcome the difficulty of surface effects on the emissivity of the horizontally polarized component.

A. Approach

Our approach makes use of the 85-GHz channels because the horizontally polarized 85-GHz data are much less affected by surface effects than the horizontally polarized 19-GHz data [15], and the 85-GHz channels have successfully been used in sea ice concentration retrievals under clear atmospheric conditions [12]. Here we use the 85-GHz channels together with a forward

radiative transfer model to provide ice concentrations under all atmospheric conditions.

Starting with the NASA Team $PR(19) - GR(37V 19V)$ domain [Fig. 1(a)], we rotate the axes by ϕ_{19}, the angle between the GR-axis and the A–B line (FY–MY line for the Arctic). With the A–B line now vertical, the rotated PR, PR_R, defined by

$$PR_R(19) = -GR(37V 19V)\sin \phi_{19} + PR(19)\cos \phi_{19} \quad (3)$$

is independent of ice types A and B as defined by the tiepoints shown in Fig. 1(a). A similar rotation is also done in the $PR(85) - GR(37V 19V)$ domain (not shown). The angles expressed in radians are given in Table I.

Next, we make use of $GR(85V 19V)$ and $GR(85H 19H)$ to resolve the ambiguity between pixels with true low ice concentration and pixels with significant surface effects. A plot of these two ratios is found to form narrow clusters, except for areas where surface effects decrease $TB(19H)$ and consequently increase $GR(85H 19H)$ [Fig. 1(b)]. Values of high $GR(85V 19V)$ and high $GR(85H 19H)$ are indicative of open water. The range of $GR(85H 19H)$ values is larger because of the greater dynamic range between ice and water for the horizontally polarized components. With increasing ice concentration, the two ratios have more similar values [Fig. 1(b)]. The narrow cluster of pixels adjacent to the diagonal shown in Fig. 1(b) represents 100% ice concentration with different GR values corresponding to different ice types. When surface effects come into play, points deviate from this narrow cluster toward increased $GR(85H 19H)$ values (cloud of points to the right of the diagonal), while $GR(85V 19V)$ remains constant. This cloud of points labeled C in Fig. 1(b) also corresponds to the cluster of points labeled C in Fig. 1(a). Therefore, the difference between these two variables

$$\Delta GR = GR(85H 19H) - GR(85V 19V) \quad (4)$$

will be used in the retrieval of ice concentration as an indicator of the presence of ice type C.

Finally, we need a third parameter to avoid the ambiguity between changes in ice concentration and changes in atmospheric conditions because of the higher sensitivity of the 85-GHz channels to atmospheric variability compared to the lower frequency channels. This third parameter is the rotated $PR(85)$, $PR_R(85)$, computed from the $PR(85) - GR(37V 19V)$ domain, analogous to the calculation of $PR_R(19)$ (Table I). In Fig. 2, ΔGR is plotted against $PR_R(19)$ [Fig. 2(a)] and $PR_R(85)$ [Fig. 2(b)] for the same region of the Weddell Sea as used for Fig. 1. Two primary clusters can be identified in each plot. One cluster with high PR and ΔGR values is representative of open water with increasing weather resulting in lower PR_R values. The other cluster with low PR_R and ΔGR values are pixels with high ice concentrations. The cloud of points in the NASA Team $PR - GR$ domain associated with surface effects (labeled C in Fig. 1) has now become a linear cluster. Ice without surface effects has $PR_R(19)$ and ΔGR values close to zero. $PR_R(19)$ and ΔGR increase with increasing surface effects. In agreement with the results from Mätzler et al. [15], $PR_R(85)$ is nearly independent of surface effects, resulting in an almost vertical cluster of points. Ice type C, which lies near the top end of the cluster and represents ice with a large
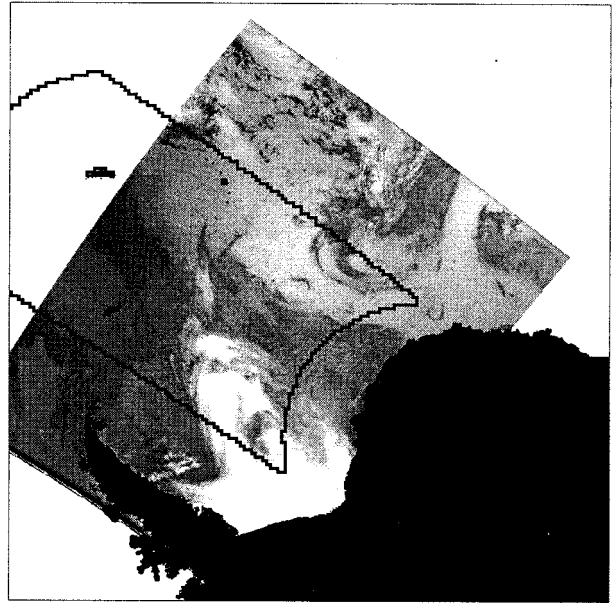

Fig. 4. DMSP OLS infrared data for September 12, 1992, corresponding to the region labeled SA in Fig. 3. The black contour corresponds to the coincident SSM/I swath as shown in Fig. 5. The black area is the Antarctic continent.

amount of surface effects, is a radiometrically distinct ice type in this rotated domain. The scatter of points results partially from weather effects, partially from the natural variability in emissivity, and partially from real ice concentration changes.

B. Atmospheric Correction

In order to investigate quantitatively how different atmospheric conditions affect the retrievals, we calculated brightness temperatures for each SSM/I channel using a forward atmospheric radiative transfer model [11] for each of the three ice types and open water. The model was run for different sea surface temperatures, atmospheric temperature and humidity profiles, and cloud conditions. The model considers absorption by water vapor and atmospheric oxygen as well as absorption and scattering by liquid and frozen hydrometeors. Model inputs are

1) climatological winter and summer atmospheric temperature and humidity profiles from the Antarctic Georg-von-Neumayer station [10];
2) surface emissivities from Eppler et al. [5] adjusted to match the observed ratios under clear atmospheric conditions;
3) temperatures of the emitting surface:
   Open water: 271K;
   Sea ice, summer: 268K;
   Sea ice, winter: 248K.
4) different cloud types from cirrus to cumulus congestus taken from Fraser et al. [6].

The various atmospheric conditions used are presented in Table II.

The modeled $PR_R(19)$, $PR_R(85)$, and ΔGR values for different atmospheres over the three pure surface types are overlain in Fig. 2 as gray circles. The figure shows that the model results
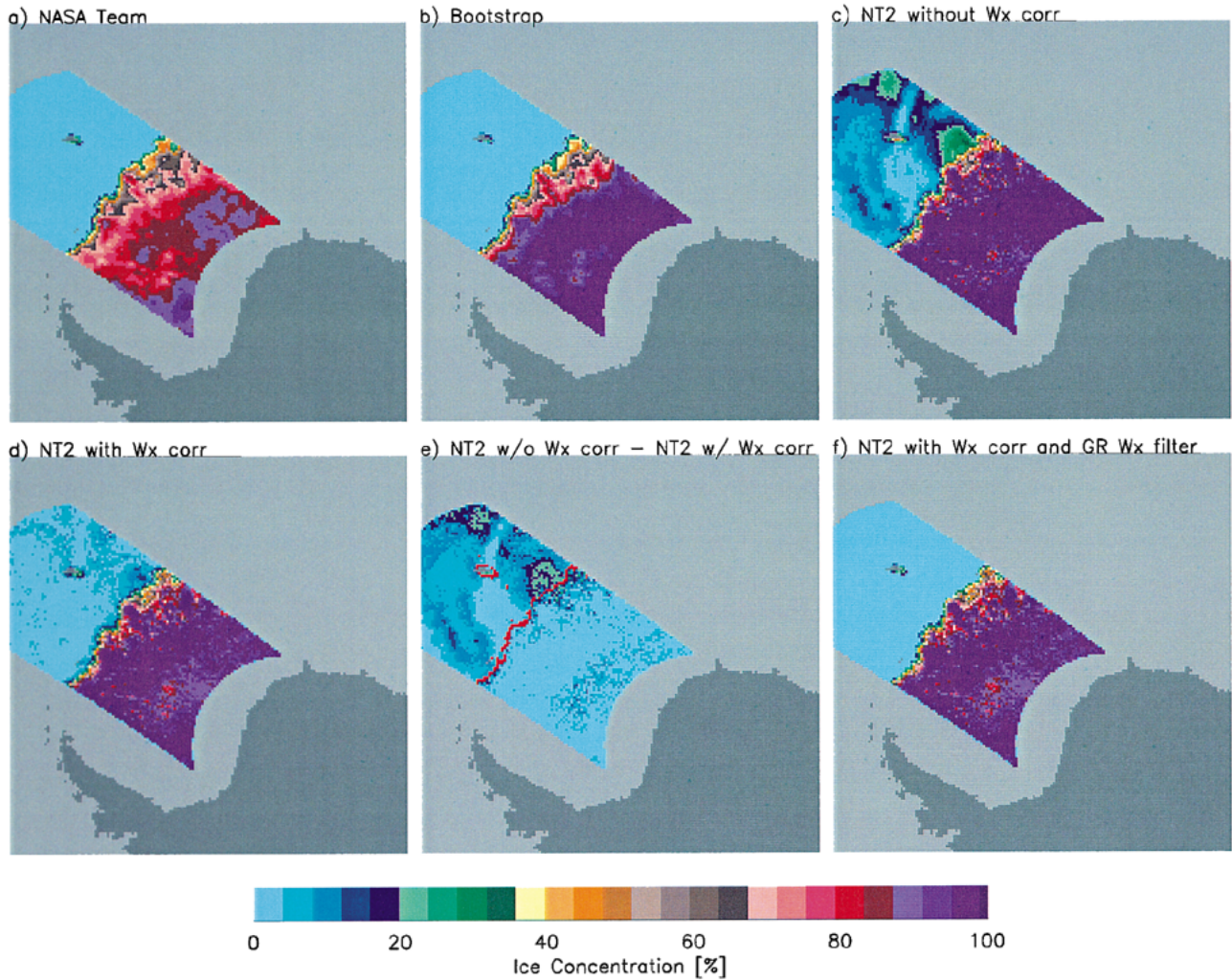
Fig. 5. SSM/I-derived ice concentrations from a DMSP F-10 overflight for September 12, 1992. Ice concentrations using (a) the NT and (b) the BS algorithms. (c) Ice concentrations using the NT2 algorithm without atmospheric correction and (d) with atmospheric correction. Difference between the NT2-derived ice concentration (e) without and with atmospheric correction (the red line indicates the ice edge). Final NT2 ice concentration using (f) the NT GR weather filter.

in most cases span the width of the observed clusters. Clear atmosphere results have the lowest ΔGR and highest PR_R values for each surface type. As shown by Maslanik [14] for the Arctic and Oelke [16] for the Antarctic, weather effects on the NT algorithm result in significant changes in ice type but not in total ice concentration for consolidated ice. This is reflected both in the vertical orientation of the gray circles and in the relatively tight ice cluster in the $PR_R(19) - \Delta GR$ plot. In contrast, the model results show a decrease in the $PR_R(85)$ plot with increasing weather explaining in part the broader ice cluster.

Using the radiative transfer model, we compute brightness temperatures for each SSM/I channel and calculate $\langle PR_R(19)\rangle$, $\langle PR_R(85)\rangle$, and $\langle \Delta GR\rangle$, which are matrices containing all combinations of ice concentration (0–100% in 1% increments) and all atmospheric conditions used (Table II). Both the ice concentration and the atmospheric contribution are found by locating the minimum of the quantity δR, defined by

$$\delta R = (PR_{Ri}(19) - \langle PR_R(19)\rangle)^2 + (PR_{Ri}(85) - \langle PR_R(85)\rangle)^2 + (\Delta GR_i - \langle\Delta GR\rangle)^2 \quad (5)$$

TABLE III
CALCULATED ICE CONCENTRATIONS RESULTING FROM CHANGES OF ±1K IN BRIGHTNESS TEMPERATURE FOR EACH CHANNEL. THE BOTTOM ROW IS THE RSS CHANGE FOR ALL CHANNELS

Δ K	C=32% +1 K	C=32% −1 K	C=51% +1 K	C=51% −1 K	C=98% +1 K	C=98% −1 K
19V	34	31	52	49	99	95
19H	32	32	51	51	98	98
37V	31	33	50	52	95	99
85V	30	34	49	53	94	100
85H	34	30	45	48	100	94
$\sqrt{\sum_i(\Delta C_i)^2}$	3.6	3.2	6.5	4.2	5.3	5.5

where $PR_{Ri}(19)$, $PR_{Ri}(85)$, and ΔGR_i are the ratios calculated from the observed brightness temperatures for a pixel i. Bracketed parameters indicate the modeled ratios.

III. RESULTS

A. Hemispheric Retrievals

Examples of wintertime ice concentration retrievals are shown in Fig. 3 for the northern and southern hemispheres

using the NT, the BS, and the NT2 algorithms. In the Arctic, the NT2 algorithm appears to give generally higher ice concentrations in areas of the central Arctic and in the seasonal sea ice zones. As mentioned earlier, differences between the NT and BS algorithms are much larger in the Antarctic. One can clearly identify the areas of lower ice concentrations in the outer pack in the NT results (compared to the BS results), which result from the aforementioned surface effects. On the other hand, the BS results give lower ice concentrations in the vicinity of the Antarctic continent, resulting from the algorithm's sensitivity to physical temperature change. To some extent, the higher concentrations of the BS algorithm in the outer pack may also result from its temperature sensitivity. Neither of these deficiencies is apparent in the NT2 results. Detailed comparison with other data sets will be presented in Section IV.

B. Reduction of Weather Effects

The effectiveness of the NT2 algorithm in reducing atmospheric effects both over the open ocean and in the marginal ice zone is illustrated by a comparison of SSM/I ice concentration retrievals with infrared data from the optical linescan system (OLS) onboard DMSP satellites. The appropriateness of the DMSP OLS is that it provides measurements spatially and temporally coincident with the SSM/I. Here, we use an OLS image from an overflight of the DMSP F-10 satellite for November 12, 1992 over the Weddell Sea (Fig. 4). Most cloud-covered regions can be identified by their bright swirly patterns. In Fig. 5, the results from the NT and BS algorithms are presented for the same region shown in Fig. 4. Using the new algorithm without the atmospheric model, the effect of weather is clearly visible over the open ocean [Fig. 5(c)]. Using the atmospheric model [Fig. 5(d)], the weather patterns over the ocean are greatly reduced. In the marginal ice zone, clouds lead to higher ice concentration without the weather correction but with the weather correction, the ice concentrations are reduced. The difference map [Fig. 5(e)] shows significant reductions in ice concentration for the open ocean and in portions of the marginal ice zone where clouds can be identified in the OLS image (Fig. 4). The remaining erroneous ice concentrations over the open ocean ($<20\%$) [Fig. 5(d)] may be the result of wind roughening and are easily eliminated using GR weather filters as used in the NT algorithm [Fig. 5(f)].

Although these results suggest that the atmospheric contribution to the brightness temperatures at 85 GHz can be accounted for, very heavy cloud conditions can prevent the radiation emitted from the surface at 85 GHz from reaching the sensor. Analysis of both summer and winter retrievals shows that pixels exhibiting opaque conditions amount to less than 0.1%. For the open ocean, the NT GR weather filters are used so that extreme weather conditions are filtered beforehand.

C. Sensitivities to Noise and Atmospheric Variations

In order to investigate how sensor noise affects the ice concentration retrievals, we vary the brightness temperatures for each SSM/I channel by ± 1K, the upper limit of sensor noise [8]. This is done for three sets of brightness temperatures corresponding to ice concentrations of 32%, 51%, and 98% in order
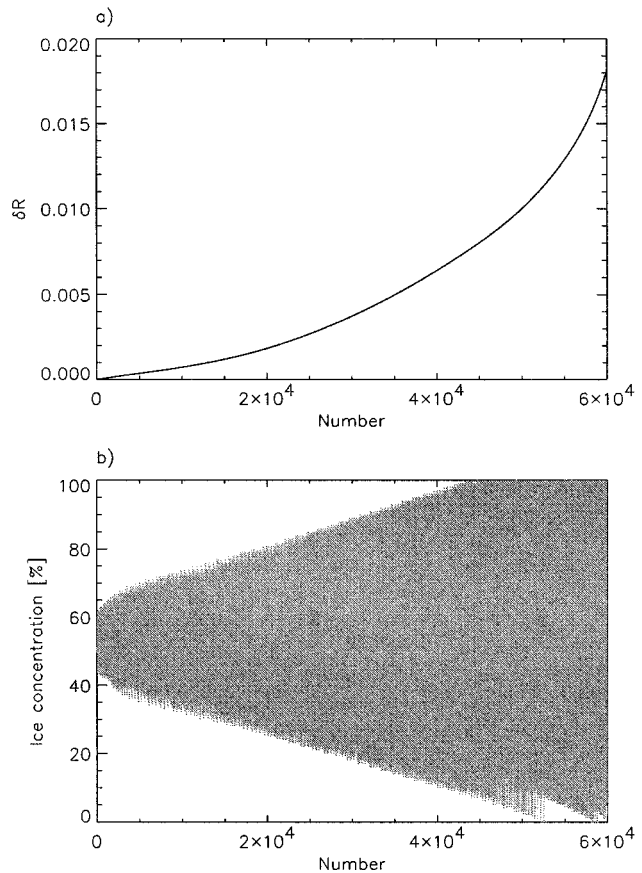

Fig. 6. (a) All of the possible 60 000 δR values (sorted by increasing δR value) and (b) the corresponding ice concentrations for a retrieved ice concentration of 51%.

TABLE IV
ICE CONCENTRATIONS WITH THE SMALLEST δR FOR EACH ATMOSPHERE
SEPARATELY FOR THE 32%, 51%, AND 98% CASES

Atm. Idx	C=32%		C=51%		C=98%	
	IC	δR	IC	δR	IC	δR
0	40	2.5E-5	61	7.0E-5	96	1.4E-6
1	44	1.2E-4	64	1.7E-4	98	1.3E-6
2	34	1.6E-6	58	1.2E-5	93	3.9E-6
3	39	6.6E-5	61	1.2E-4	96	2.0E-6
4	37	3.0E-6	60	1.5E-5	94	2.3E-6
5	42	3.4E-5	63	8.0E-5	97	2.3E-6
6	29	6.1E-5	51	1.6E-6	94	5.5E-5
7	32	1.8E-7	59	3.3E-6	94	1.5E-5
8	28	4.1E-4	44	9.7E-6	94	1.6E-4
9	29	8.4E-5	51	3.2E-7	94	7.8E-5
10	23	1.4E-3	40	3.1E-4	94	4.1E-4
11	23	8.9E-4	41	1.3E-4	94	3.0E-4

to represent a wide range of ice conditions. The results are presented in Table III and are approximately the same order of magnitude as for the NT algorithm [21]. These noise sensitivity coefficients may also be used to estimate the effect of surface emissivity variations on the algorithm retrievals.

Next, to understand how the limited set of atmospheres used in the algorithm may affect the retrievals, we investigate three pixels with ice concentrations of 32%, 51%, and 98% analogous to the study of sensor noise. The variable δR from (5) provides
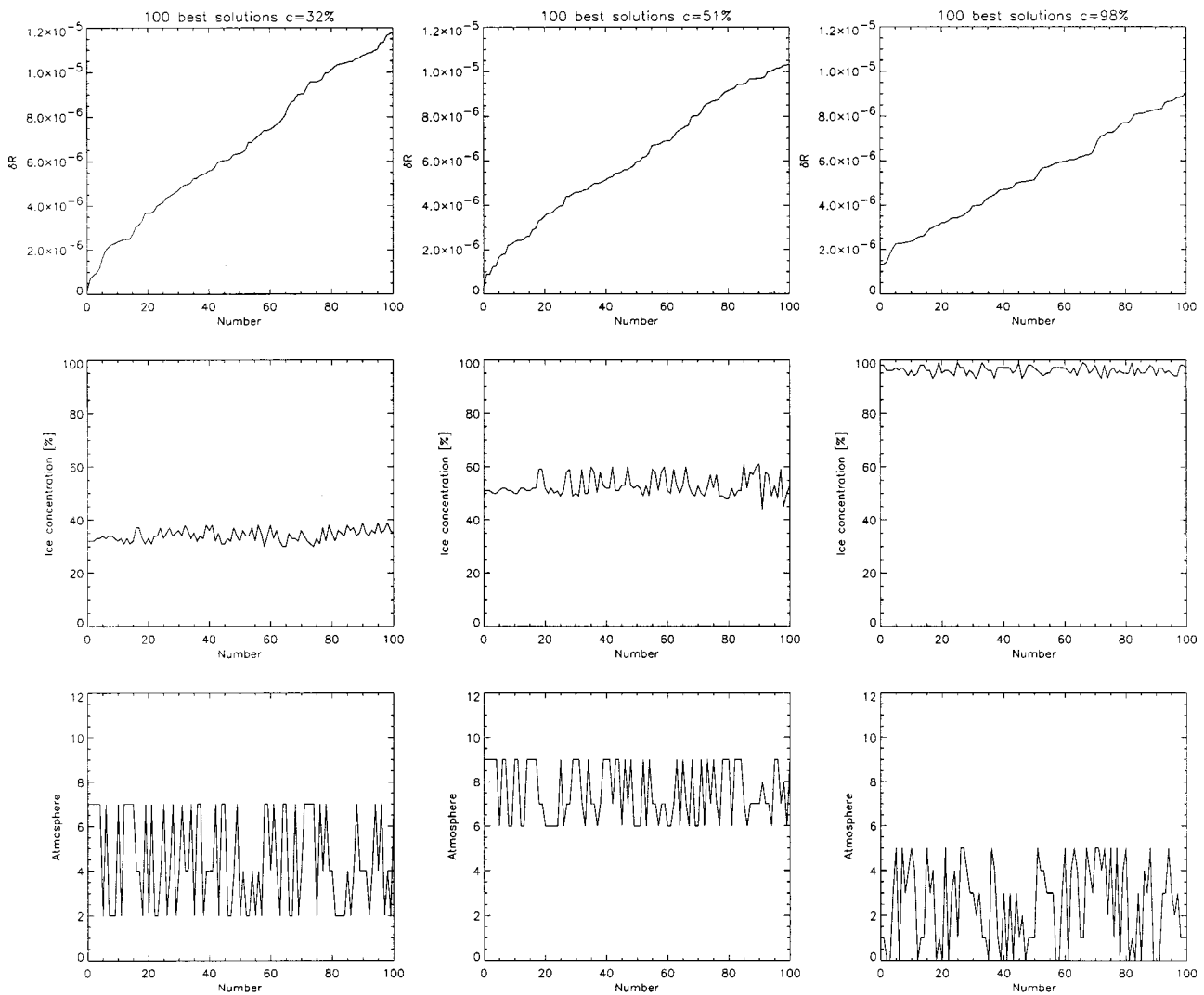
Fig. 7. Smallest 100 δR's with corresponding ice concentrations and atmospheric indices for the 32% case (left column), the 51% case (middle column), and the 98% case (right column).

a measure of the difference between the measured set of ratios and the modeled ratios for each ice concentration and atmosphere combination. The values of δR are sorted by increasing difference. These, together with the corresponding ice concentrations, are plotted in Fig. 6. Fig. 6(a) shows that δR reaches a distinct minimum and that the ice concentrations converge to an ice concentration of about 50% [Fig. 6(b)]. In Fig. 7, the smallest 100 δR values, together with the corresponding ice concentrations and atmospheric indices for the 32%, 51%, and 98% cases, are presented. For the 32% and 51% cases, δR is almost zero for the best solution, meaning that there exists a set of modeled ratios that matches the measured ratios almost perfectly. For the 98% case, the best δR is somewhat higher. For the 15 smallest differences, the ice concentrations vary only by ± 2% for the 32% and 98% cases and by ± 1% for the 51% case. Although the total ice concentrations are very stable for the last 15 solutions, oscillations in the atmospheric indices (Table II) continue. For example, in the 32% case, oscillations occur between the atmospheric index 2 and 7, which represents a summer atmosphere with cirrus clouds (high water vapor, low cloud liquid water) and a winter atmosphere with more liquid water and less
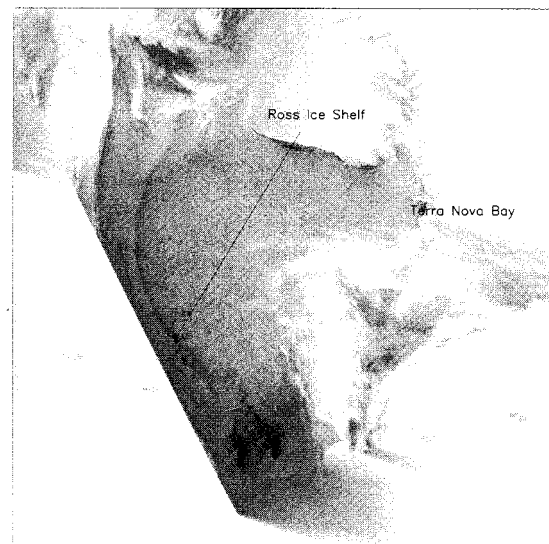

Fig. 8. AVHRR infrared image of the Ross Sea coincident with the data in Fig. 3 (Box SB). Ice concentrations were calculated along the transect, shown in black.
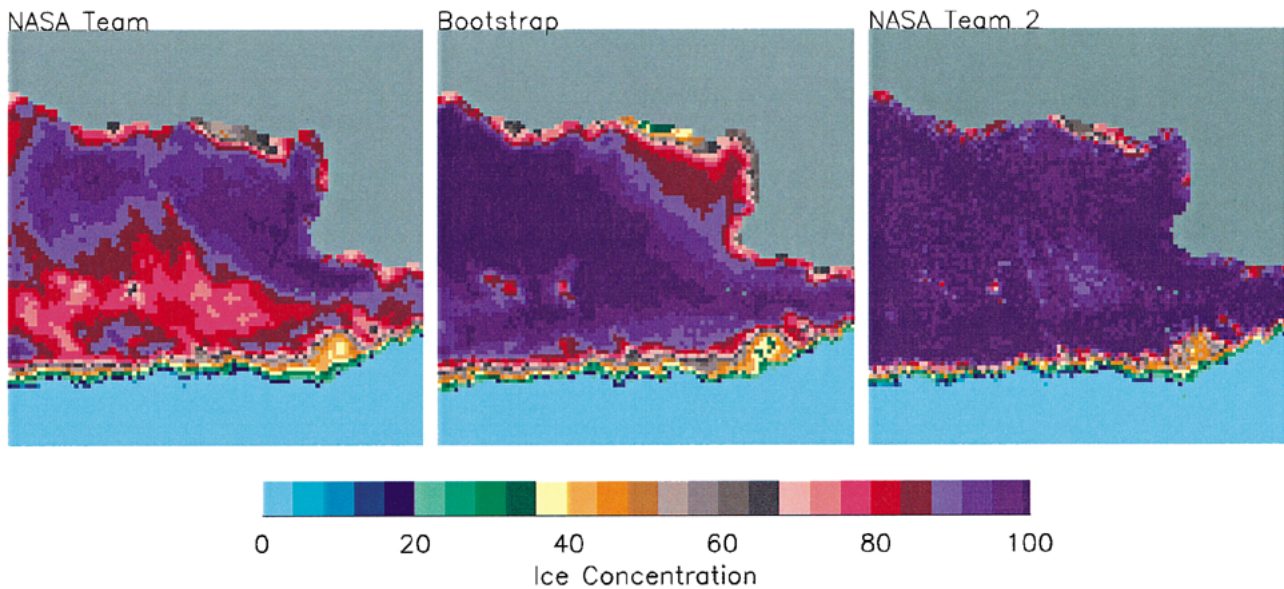
Fig. 9.   Subset of Fig. 3 for the Ross Sea (Box SB).

water vapor. Similar phenomena can be seen for the 51% and 98% cases. Other cases have been found where the atmospheric index oscillates between two odd or even values that correspond to the same season. This suggests that for those cases, the "true" atmosphere has probably a liquid water content between the two modeled atmospheres. Because all of the SSM/I channels (except for the 22-GHz channel) lie in atmospheric "window" frequencies, the atmospheric contribution is generally rather small (even at 85 GHz). Therefore, we cannot retrieve atmospheric parameters over the highly emissive sea ice, but we can reduce the "atmospheric noise" in the received radiances.

In Table IV, the ice concentrations with the smallest δR value for each atmospheric index (see Table II) are listed separately. For the 32% case, the smallest δR corresponds to an atmosphere index of 7 followed by indices 2 and 4, which all have similar ice concentrations. The δR value is about an order of magnitude smaller for index 7 compared to indices 2 and 4. The range in ice concentration is approximately $\pm 10\%$, indicating the error range without atmospheric correction. This also agrees with the magnitude of the differences observed in Fig. 5(e). The 51% case has about the same range. Here, δR is high for small atmospheric indices and has a distinct minimum at index 9 followed by index 6, which both give identical ice concentrations. The range in ice concentrations is smaller for the 98% case ($\pm 5\%$), with smallest δR values for atmospheres with little liquid water content. Based on these analyses, we conclude that the atmospheric correction is necessary and that the retrieved ice concentration is stable.

IV. COMPARISONS WITH OTHER DATA SETS

The results of the NT2 algorithm are verified through a comparison with analyses from other data sources. For cloud-free conditions, this can be done with high resolution visible or infrared data from the NOAA AVHRR instrument. Because of the absence of solar illumination during the winter season, only infrared data can be used during this period.
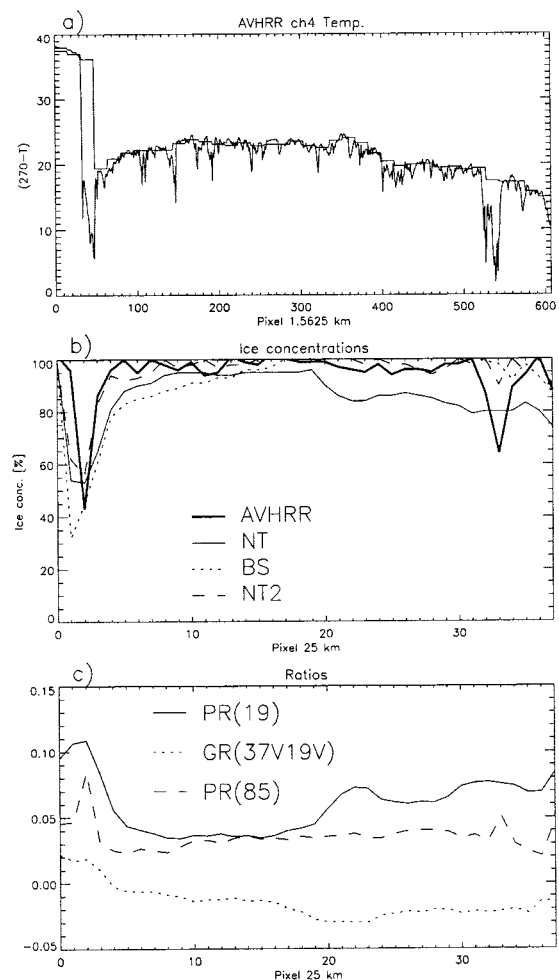

Fig. 10.   Transect through the Ross Sea (black line in Fig. 10). AVHRR infrared temperature data and reference 100% ice concentration temperatures derived from 16×16 pixels boxes. (b) Ice concentrations derived from SSM/I data using the NT, BS, and NT2 algorithms as well as (c) the AVHRR concentrations brightness temperature ratios.
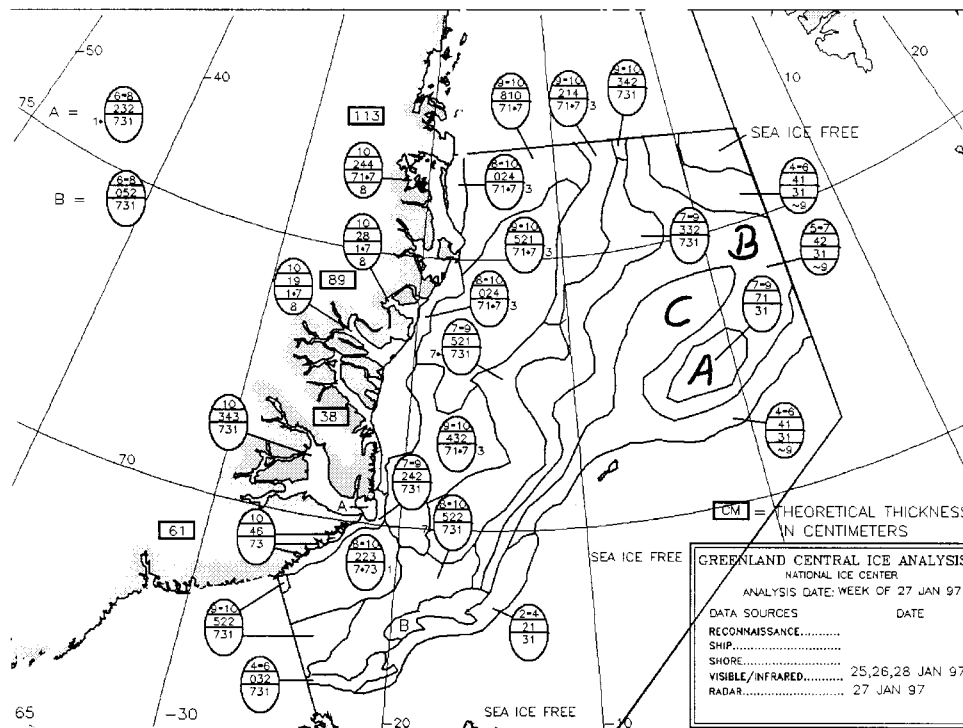
Fig. 11. Ice chart from the National Ice Center coincident with the data in Fig. 3. The total ice concentration (or range of) for each polygon is indicated in the uppermost group of the ice chart symbology, expressed in tenths.

TABLE V
CORRELATION COEFFICIENT AND AVERAGE DIFFERENCE BETWEEN THE ICE
CONCENTRATIONS FROM AVHRR AND EACH OF THE THREE SSM/I
ALGORITHMS FOR THE ROSS SEA TRANSECT, AS PLOTTED IN Fig. 10(b)

Algo.	Corr.Coeff.	$\overline{C_{AVHRR} - C_{SSM/I}}$
NT	0.65	7.9
BS	0.50	2.2
NT2	0.83	-0.8

For the comparison with infrared data, high resolution AVHRR LAC data have been gridded to a 1.5625 km SSM/I grid. A problem when using infrared data is that the regional variability of air and surface temperatures prohibits the calculation of AVHRR ice concentration using simple thresholds. To overcome this problem, the minimum temperature for a 16×16 1.5625-km pixel box (equivalent to 25×25 km) plus 0.5K (which is about the standard deviation in AVHRR surface temperature for consolidated ice) is taken to represent the 100% ice concentration temperature. The open water temperature is assumed to be 271.2K. Ice concentrations are then calculated using a linear relationship between these two temperatures and the measured temperature.

A. Antarctic

A mostly cloud-free AVHRR image of the Ross Sea for the same day shown in Fig. 3 is presented in Fig. 8. Except for a narrow coastal polynya along the Ross Ice Shelf and in Terra Nova Bay, the sea ice is highly consolidated, although it contains numerous leads. A blow-up of the Ross Sea (Fig. 9) shows

that the NT algorithm seems to underestimate ice concentration in the outer pack and the BS algorithm seems to underestimate in the vicinity of the ice shelf (indicative of the deficiencies discussed above and in Comiso *et al.* [4]), whereas in the NT2 algorithm, these deficiencies are not apparent. Analysis along a transect (black line in Fig. 8) from the ice shelf toward the outer pack provides a more quantitative measure of the observed differences. In Fig. 10(a), we plot the difference between 271.2K and the AVHRR channel-4 temperatures. The horizontal line segments represent the derived ice temperatures corresponding to a 100% ice concentration for each 16×16 pixel box. After the coastal polynya (pixel 60) adjacent to the shelf (pixels 0–30), the temperature decreases gradually until pixel 100. Leads can be identified as sharp drops in the temperature record. From about pixel 520 to pixel 550, some small polynyas have opened that are also recognizable in the AVHRR image (Fig. 8). The 25-km ice concentrations [Fig. 10(b)] all capture the coastal polynya, but only the NT2 algorithm shows a rapid increase in ice concentration in agreement with the AVHRR concentrations. In general, the NT2 retrievals provide the best match with the AVHRR concentrations. This good agreement is also reflected in the correlation coefficient of 0.83 [compared to 0.65 for the NT and 0.50 for the BS algorithms (Table V)]. The small average difference of -0.8% (Table V) shows that the bias is almost insignificant. The better performance of the NT2 algorithm compared to the other two can be explained with the help of the $PR(19)$, $GR(37V19V)$, and $PR(85)$ values [Fig. 10(c)]. Only at $PR(85)$ do the two polynya areas result in distinct peaks. From pixel 5 to pixel 20, $PR(19)$ is fairly constant, whereas $GR(37V19V)$ decreases from 0.0 to -0.03. This decrease in
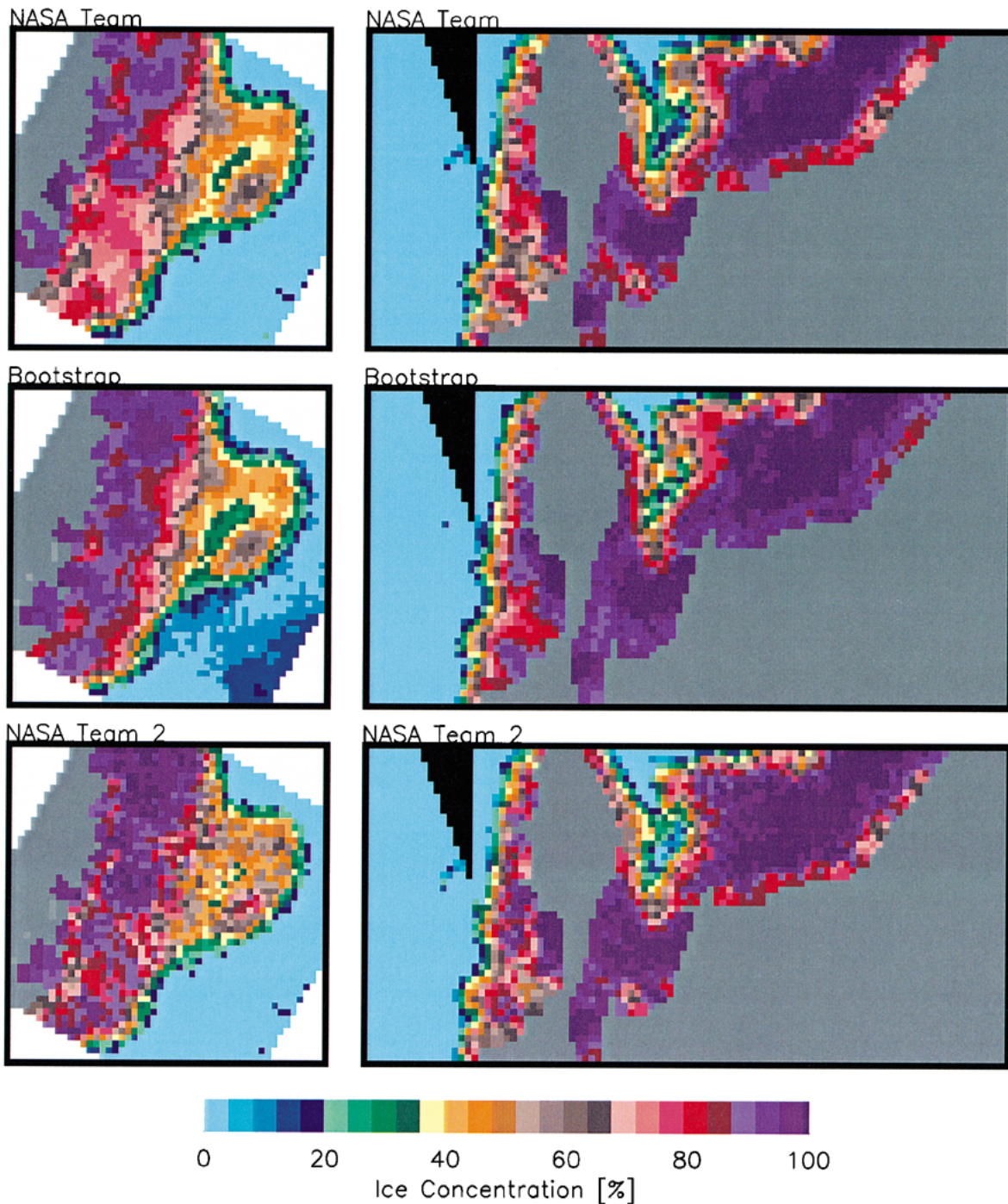
Fig. 12.   Left column: Subset of Fig. 3 for the Greenland Sea (Box NA) on January 27, 1997. Right column: SSM/I-derived ice concentrations for the Sea of Okhotsk (Box NB) on February 4, 1995.

$GR(37V19V)$ indicates a probable increase in snow cover resulting in the warming of the snow–ice interface. This may also explain the increase in BS ice concentrations from pixel 4 to pixel 17, because of the algorithm's temperature sensitivity. At pixel 20, the NT ice concentrations begin to decrease as a result of an increase in $PR(19)$. Because $GR(37V19V)$ stays at values well below zero, this increase in $PR(19)$ is probably caused by snow cover effects. This increase is not seen in $PR(85)$.

B. Arctic

An ice concentration chart of the Greenland Sea from the National Ice Center is presented in Fig. 11 for comparison with the SSM/I retrievals. This ice chart corresponds to the area labeled NA in Fig. 3. As one can see from the chart legend, the ice concentrations are derived from visible/infrared and radar images, giving an estimate not dependent on SSM/I data. The three SSM/I retrievals are shown in Fig. 12 (left column). In general, the three algorithms give similar results, but there are

TABLE VI
CORRELATION COEFFICIENT AND AVERAGE DIFFERENCE BETWEEN THE ICE
CONCENTRATIONS FROM AVHRR AND EACH OF THE THREE SSM/I
ALGORITHMS FOR THE SEA OF OKHOTSK TRANSECT AS PLOTTED IN Fig. 14(b)

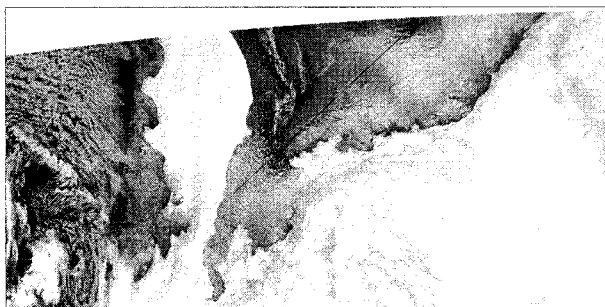| Algo.	Corr.Coeff.	$\overline{C_{AVHRR} - C_{SSM/I}}$
NT	0.71	1.6
BS	0.65	−7.2
NT2	0.74	−1.1

Fig. 13. AVHRR infrared image for the Sea of Okhotsk on February 4, 1995. The area corresponds to box NB in Fig. 3. Ice concentrations were calculated along the transect, shown in black.
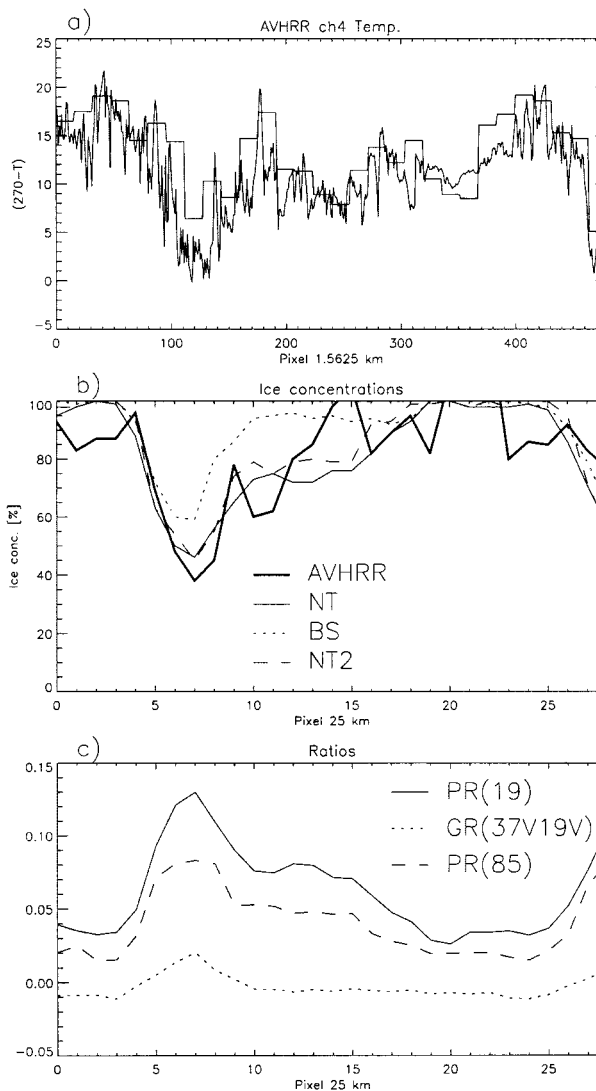
Fig. 14. Transect through the Sea of Okhotsk (black line in Fig. 13) for February 4, 1995. (a) AVHRR infrared data and reference 100% ice concentration temperatures derived from 16 × 16 pixel boxes, (b) ice concentrations derived from the SSM/I data using the NT, BS, and NT2 algorithms as well as the AVHRR concentrations, and (c) brightness temperature ratios.

significant local differences. For example, at the southern part of the Odden sea ice tongue (label A in Fig. 11), the ice concentrations are higher in the NT2 results (70–80%) compared to the NT and the BS results (60–70%). Also, for the areas labeled B and C in Fig. 11, the NT2 results show better agreement with the NIC ice chart than do either of the NT and BS results.

An Arctic seasonal sea ice zone for which we have a cloud-free AVHRR scene is the Sea of Okhotsk. The February 4, 1995 AVHRR image is shown in Fig. 13. The corresponding SSM/I-derived ice concentrations are presented in Fig. 12 (right column). Overall, the three ice concentration algorithms give similar results. A transect was chosen to avoid cloudy areas (black line in Fig. 13) and the ice concentrations derived (Fig. 14) as was done for the Ross Sea. Because the AVHRR surface temperatures are much more variable than in the Ross Sea transect, the standard deviation for consolidated ice was 3K, which was again added to the minimum temperature for each 16 × 16 pixel box and assumed to be representative of the 100% ice concentration temperature [Fig. 14(a)]. All of the algorithms resolve the open water at pixel 7, but are in rather poor agreement with the AVHRR concentrations from pixel 10 on [Fig. 14(b)]. While the reason for this is uncertain, we suspect that unresolved clouds in the image cause the AVHRR ice temperature peaks observed in Fig. 14(a) and result in underestimates of ice concentration by the AVHRR algorithm. For example, the peak between pixels 170 and 180 in Fig. 14(a) results in the AVHRR ice concentration drop at pixels 10 and 11 shown in Fig. 14(b). The ratios shown in Fig. 14(c) reflect the general variation in sea ice concentrations observed by all the SSMI algorithms. Although the correlation coefficients are lower for all algorithms than they were for the Ross Sea transect (Table VI), the NT2 algorithm still gives the highest correlation coefficient and the smallest bias.

V. SUMMARY

An enhanceMENT OF THE NASA Team sea ice concentration algorithm is presented. The algorithm has the same functional form as the original NT algorithm, but uses a wider range of frequencies (19–85 GHz) to overcome the problem of surface snow effects on the horizontal polarized 19-GHz channel, which are particularly apparent in Southern Ocean sea ice retrievals. The algorithm accommodates ice temperature variability through the use of radiance ratios as in the original NT algorithm and has the added advantage of providing weather-corrected sea ice concentrations through the utilization of a forward atmospheric radiative transfer model. The new retrievals of sea ice concentration for both the Arctic and Antarctic do not reveal the deficiencies present in the NT and BS algorithms discussed previously by Comiso et al. [4]. Quantitative comparisons with infrared AVHRR data show that

the new algorithm provides more accurate ice concentrations with much less bias than the other two algorithms. Finally, the planned use of this algorithm with the EOS AQUA advanced microwave scanning radiometer (AMSR) should provide a rich source of information on the highly variable polar sea ice packs given that the AMSR spatial resolution will be about twice that of the SSM/I.

ACKNOWLEDGMENT

REFERENCES

[1] D. J. Cavalieri, "A microwave technique for mapping thin sea ice," *J. Geophys. Res.*, vol. 99, pp. 12 561–12 572, 1994.

[2] D. J. Cavalieri, P. Gloersen, and W. J. Campbell, "Determination of sea ice parameters with the NIMBUS 7 scanning multichannel microwave radiometer," *J. Geophys. Res.*, vol. 89, pp. 5355–5369, 1984.

[3] J. C. Comiso, "SSM/I sea ice concentrations using the bootstrap algorithm," *NASA Ref. Pub.,1380*, p. 49, 1995.

[4] J. C. Comiso, D. J. Cavalieri, C. L. Parkinson, and P. Gloersen, "Passive microwave algorithms for sea ice concentration—A comparison of two techniques," *Remote Sens. Environ.*, vol. 60, pp. 357–384, 1997.

[5] D. T. Eppler *et al.*, "Passive microwave signatures of sea ice," in *Microwave Remote Sensing Sea of Ice, Geophysics Monograph Ser.*, F. Carsey *et al.*, Ed. Washington, DC: AGU, 1992, vol. 68, pp. 47–71.

[6] R. S. Fraser, N. E. Gaut, E. E. Reifenstein, and H. Sievering, "Interaction mechanisms—Within the atmosphere," in *Manual of Remote Sensing*, R. G. Reeves, A. Anson, and D. Landen, Eds. Falls Church, VA: American Society of Photogrammetry, 1975, pp. 181–233.

[7] P. Gloersen and D. J. Cavalieri, "Reduction of weather effects in the calculation of sea ice concentration from microwave radiances," *J. Geophys. Res.*, vol. 91, pp. 3913–3919, 1986.

[8] J. Hollinger, R. Lo, G. Poe, R. Savage, and J. Pierce, *Special Sensor Microwave/Imager User's Guide*. Washington, DC: Naval Res. Lab., 1987.

[9] T. Hunewinkel, T. Markus, and G. C. Heygster, "Improved determination of the sea ice edge with SSM/I data for small-scale analyzes," *IEEE Trans. Geosci. Remote Sensing*, vol. 36, pp. 1795–1808, Sept. 1998.

[10] G. König-Langlo, "The meteorological data of the Georg-von-Neumayer-Station (Antarctica) for 1988, 1990, 1991," in *Tech. Rep. Polar Research*. Bremerhaven, Germany: Alfred-Wegener-Instiut für Polar- und Meeresforschung, 1992, p. 70.

[11] C. Kummerow, "On the accuracy of the Eddington approximation for radiative transfer in the microwave frequencies," *J. Geophys. Res.*, vol. 98, pp. 2757–2765, 1993.

[12] D. J. Cavalieri, C. Garrity, R. O. Ramseier, and R. H. Whritner, "Total sea ice concentration retrieval from the SSM/I 85.5 GHz channels during the Arctic summer," *Remote Sens. Environ.*, vol. 62, pp. 63–76, 1997.

[13] T. Markus and B. A. Burns, "A method to estimate sub-pixel scale coastal polynyas with satellite passive microwave data," *J. Geophys. Res.*, vol. 100, pp. 4473–4487, 1995.

[14] J. A. Maslanik, "Effects of weather on the retrieval of sea ice concentration and ice type from passive microwave data," *Int. J. Remote Sensing*, vol. 13, pp. 34–57, 1992.

[15] C. Mätzler, R. O. Ramseier, and E. Svendsen, "Polarization effects in sea-ice signatures," *IEEE J. Oceanic Eng.*, vol. OE-9, pp. 333–338, 1984.

[16] C. Oelke, "Atmospheric signatures in sea-ice concentration estimates from passive microwave: modeled and observed," *Int. J. Remote Sensing*, vol. 18, pp. 1113–1136, 1997.

[17] K. M. St. Germain, "A two-phase algorithm to correct for atmospheric effects on the 85 GHz channels of the SSM/I in the Arctic region," in *Proc. IGARSS'94*, Pasadena, CA, 1994, pp. 148–151.

[18] K. Steffen, J. Key, D. J. Cavalieri, J. C. Comiso, P. Gloersen, K. St. Germain, and I. Rubinstein, "The estimation of geophysical parameters using passive microwave algorithms," in *Microwave Remote Sensing of Sea Ice, Geophysics Monograph Ser.*, F. Carsey, Ed. Washington, DC: AGU, 1992, vol. 68, pp. 201–231.

[19] M. Sturm, K. Morris, and R. Massom, "The character and distribution of the winter snow cover on the sea ice of the Bellingshausen, Amundsen, and Ross Seas, Antarctica, 1994-1995," in *Antarctic Sea Ice: Physical Processes, Interactions, and Variability, Antarctic Research Ser.*, M. O. Jeffries, Ed. Washington, DC: AGU, 1998, vol. 74, pp. 1–18.

[20] E. Svendsen, C. Mätzler, and T. C. Grenfell, "A model for retrieving total sea ice concentration from a spaceborne dual-polarized passive microwave instrument operating at 90 GHz," *Int. J. Remote Sensing*, vol. 8, pp. 1479–1487, 1987.

[21] C. T. Swift and D. J. Cavalieri, "Passive microwave remote sensing of sea ice research," *EOS*, vol. 66, pp. 1210–1212, 1985.

[22] H. J. Zwally, J. C. Comiso, C. L. Parkinson, W. J. Campbell, F. D. Carsey, and P. Gloersen, "Antarctic sea ice, 1973-1976: Satellite passive-microwave observations," *NASA*, p. 206, SP-459, 1983.

Thorsten Markus received the M.S. degree in 1992 and the Ph.D. degree in 1995, both in physics, from the University of Bremen, Bremen, Germany.

He was a National Research Council Resident Research Associate with NASA Goddard Space Flight Center (GSFC), Greenbelt, MD, from 1995 to 1996. He is now an Assistant Research Scientist with the NASA/GSFC, University of Maryland, Baltimore County Joint Center for Earth Systems Technology, Baltimore, MD. His research interests include satellite remote sensing and the utilization of satellite data to study oceanic and atmospheric processes. The current focus of his research is on the polar regions.

Dr. Markus is a member of the American Geophysical Union.

Donald J. Cavalieri received the B.S. degree in physics from the City College of New York in 1960, the M.A. degree in physics from Queens College of New York in 1967, and the Ph.D. degree in meteorology and oceanography from New York University in 1974.

From 1974 to 1976, he served as a National Research Council Postdoctoral Resident Research Associate with the NOAA Environmental Data Service, Boulder, CO, where he continued his doctoral research on stratospheric–ionospheric coupling. From 1976 to 1977, he was a Visiting Assistant Professor in the Department of Physics and Atmospheric Sciences, Drexel University, Philadelphia, PA, where he worked on stratospheric temperature retrievals from satellite infrared radiometers. In the fall of 1977, as a Staff Scientist with Systems and Applied Sciences Corp., Riverdale, MD, he started working on sea ice retrieval algorithms in preparation for the launch of Nimbus-7 SMMR. In 1979, he joined the Laboratory for Atmospheres, NASA Goddard Space Flight Center (GSFC), Greenbelt, MD. He is currently a Senior Research Scientist in the Oceans and Ice Branch of the Laboratory for Hydrospheric Processes, GSFC. His responsibilities include the development and validation of sea ice algorithms for the EOS-AQUA AMSR instrument. His research interests currently center on polar ocean processes and the microwave remote sensing of the cryosphere.

Dr. Cavalieri is a Member of the American Geophysical Union and the American Meteorological Society.